

Hydrodynamic simulations of pulsar glitch recovery

G. Howitt^{1*}, B. Haskell¹ and A. Melatos¹

¹*School of Physics, University of Melbourne, Parkville, Victoria, 3010, Australia*

Accepted XXXX. Received XXXX

ABSTRACT

Glitches are sudden jumps in the spin frequency of pulsars believed to originate in the superfluid interior of neutron stars. Superfluid flow in a model neutron star is simulated by solving the equations of motion of a two-component superfluid consisting of a viscous proton-electron plasma and an inviscid neutron condensate in a spherical Couette geometry. We examine the response of the model to glitches induced in three different ways: by instantaneous changes of the spin frequency of the inner and outer boundaries, and by instantaneous recoupling of the fluid components in the bulk. All simulations are performed with strong and weak mutual friction. It is found that the maximum size of a glitch originating in the bulk decreases as the mutual friction strengthens. It is also found that mutual friction determines the fraction of the frequency jump which is later recovered, a quantity known as the ‘healing parameter’. These behaviours may explain some of the diversity in observed glitch recoveries.

Key words: dense matter — hydrodynamics — stars: neutron — pulsars: general

1 INTRODUCTION

Radio pulsar glitches are sporadic jumps in the spin frequency of pulsars which occur against a background of steady electromagnetic spin down. During a glitch, the spin frequency increases by as much as one part in 10^5 (Manchester & Hobbs 2011), over a time-scale unresolvable by radio timing experiments (Dodson, Lewis & McCulloch 2007). Glitches are usually followed by a recovery period, during which some (though not necessarily all) of the increase in spin frequency is reversed, and the pulsar returns to a state of steady electromagnetic spin down (Wong, Backer & Lyne 2001; Yu et al. 2013). The impermanent part of the glitch is often fitted by multiple decaying exponentials, which can have characteristic timescales ranging from minutes to weeks for a single glitch (Dodson, McCulloch & Lewis 2002). Often, glitches are also followed by a change in the spin-down rate, which can persist for as long as the time between glitches (Yu et al. 2013).

Glitches provide a window into the interior of neutron stars and inform theoretical models of bulk nuclear matter (Link, Epstein & Lattimer 1999; van Eysden & Melatos 2010). Since the work of Baym, Pethick & Pines (1969) and Anderson & Itoh (1975), it has been widely believed that glitches originate in the superfluid interior of a neutron star; see Haskell & Melatos (2015) for a recent review of glitch models. The temperature is likely low enough for neutrons to form Cooper pairs and hence an inviscid Bose-Einstein condensate in certain regions of the interior (Baym, Bethe

& Pethick 1971). Direct evidence for superfluidity has come from recent observations of the young neutron star in the supernova remnant Cassiopeia A, whose current temperature is too high if its current cooling rate has been maintained since birth. A recent transition to a superfluid state in the interior, leading to enhanced cooling from neutrino emission, seems to be implied (Heinke & Ho 2010; Shternin et al. 2011; Page et al. 2011; Elshamouty et al. 2013).

A superfluid in a rotating container forms an array of vortices with quantized circulation, whose configuration determines the angular velocity of the superfluid as a whole (Tilley & Tilley 1990). As the pulsar spins down due to electromagnetic braking, there is a hydrodynamical lift force, called a Magnus force, which pushes the vortices out of the star. In the absence of obstructions, the Magnus force keeps the superfluid neutrons in corotation with the charge-neutral electron-proton fluid, which in turn is kept in corotation with the crust by the strong magnetic field. As the superfluid vortices pass through the crystalline crust, however, it is energetically favourable for vortex cores to overlap with crustal ions, which means that they ‘pin’ to lattice sites in the crust and decouple from the smoothly decelerating proton-electron fluid (Alpar 1977; Anderson et al. 1982; Seveso et al. 2014). Vortices also pin to magnetic flux tubes in the core (Mendell 1991; Link 2012), due to the superconducting nature of the protons in that region (Migdal 1959; Page, Geppert & Weber 2006). When a single vortex unpins, it can knock-on surrounding vortices before it repins, causing them to unpin as well — a vortex avalanche (Cheng et al. 1988; Warszawski & Melatos 2013). The dynamics of such avalanches are well-studied in terrestrial systems, such

* E-mail: ghowitt@student.unimelb.edu.au (GH)

as sandpiles and forest fires (Bak, Tang & Wiesenfeld 1987; Turcotte 1999), and also in astrophysical contexts, such as solar flares [see Watkins et al. (2015) for a review]. Recent studies of the statistical distributions of glitch sizes and waiting times between glitches find consistency between pulsar glitch data and the superfluid vortex avalanche model (Melatos, Peralta & Wyithe 2008; Warszawski & Melatos 2011, 2013; Melatos et al. 2015).

The dynamics of individual vortices is highly complex and has been studied extensively for terrestrial superfluids such as ^4He and Bose-Einstein condensates (Donnelly 1991; Fetter 2009). Such systems can be modelled microscopically using the Gross-Pitaevskii equation (GPE). While the GPE approach is feasible for small systems, it does not scale well to neutron stars, which contain $\gtrsim 10^{15}$ vortices. Moreover, the GPE describes weakly interacting systems such as Bose-Einstein condensates, rather than strongly interacting fermionic systems such as neutron stars. On the other hand, the average inter-vortex spacing is much smaller than the neutron star radius, so a neutron star superfluid can be described in the continuum, or hydrodynamic, limit. Each fluid element contains many vortices, so the rapid spatial variation of the superfluid velocity field around the vortices is smoothed, and the superfluid vorticity can be defined as a continuous quantity (Hall & Vinen 1956; Hills & Roberts 1977; Andersson & Comer 2006).

In this paper, we simulate the response of a model neutron star to glitches hydrodynamically. We start by describing the equations of motion for a two-component superfluid (section 2), then describe the system geometry and numerical method (section 3). We prepare the system in a state of differential rotation (section 4), then investigate the response of the system to glitches induced in three different ways in section 5. Firstly, we spin up the ‘crust’ (section 5.3); secondly, we recouple the two fluid components in the bulk (section 5.4); and finally, we spin up the core (section 5.5). We study all three types of glitches in regimes where the coupling between the two fluid components, called mutual friction, is either strong or weak. The response of the spin frequency to a glitch is dramatically different for each of the three glitch types. We find that mutual friction plays an important role in those glitches which originate in the bulk. The observed behaviour is discussed critically in section 6.

2 EQUATIONS OF MOTION

We model the neutron star as a system of two coupled fluids: a neutron condensate, labelled n , and a charge-neutral fluid of protons and electrons, labelled p . For the purpose of studying glitch relaxation this is an adequate description (Sidery, Passamonti & Andersson 2010; Haskell, Pizzochero & Sidery 2012; Haskell & Antonopoulou 2014), as electrons can be considered locked to the protons on length-scales larger than the electron screening length and time-scales longer than the inverse of the plasma frequency (Mendell 1991). We have the usual conservation laws for the number densities n_x ,

$$\partial_t n_x + \nabla_i (n_x v_x^i) = 0, \quad (1)$$

where $x = n, p$ indexes the constituent, i labels Cartesian components, and we adopt the Einstein convention of sum-

ming over repeated indices. The two momentum equations can be written as (Prix 2004)

$$\begin{aligned} &(\partial_t + n_x^j \nabla_j)(v_i^x + \varepsilon_x v_i^{yx}) + \nabla_i(\tilde{\mu}_x + \Phi) + \varepsilon_x v_{yx}^j \nabla_j v_i^x \\ &= (f_i + \nabla^j D_{ij}^x)/\rho_x, \end{aligned} \quad (2)$$

where ε_x is the entrainment coefficient, $\tilde{\mu}_x = \mu_x/m_x$ is the chemical potential μ_x scaled by the mass m_x of each component, $v_i^{yx} = v_i^y - v_i^x$ is the relative flow velocity, and Φ is the gravitational potential. Viscous terms are encoded in the tensor D_{ij}^x ; they are more numerous than in a single Newtonian fluid, given the additional degrees of freedom of a multi-fluid system (Andersson & Comer 2006; Haskell, Andersson & Comer 2012). The forces f_i on the right-hand side represent various other interactions between the fluids, such as the Lorentz force or, as we see below, the mutual friction force.

To simplify the problem we take both fluids to be incompressible and consider only the shear viscosity acting on the electron-proton ‘normal’ fluid (Haskell, Andersson & Comer 2012). We also neglect the effect of entrainment ($\varepsilon_x = 0$). In the crust the latter can actually be quite a poor approximation, as entrainment coefficients can be large (Chamel 2012; Andersson et al. 2012; Chamel 2013; Newton, Berger & Haskell 2015). However, in the outer core of the star it is a good approximation (Carter, Chamel & Haensel 2006).

Even with these simplifications, the problem is challenging numerically. The flow at every point is characterised by four quantities: the velocity fields of the proton-electron fluid, \mathbf{v}_p , and the superfluid neutrons \mathbf{v}_n and their respective chemical potentials, $\tilde{\mu}_p$ and $\tilde{\mu}_n$. The gravitational potential Φ is taken to be constant and absorbed in the chemical potential terms. In the isothermal, incompressible, constant density regime, the flow is described by the dimensionless equations¹

$$\frac{d\mathbf{v}_p}{dt} + (\mathbf{v}_p \cdot \nabla)\mathbf{v}_p = -\nabla\tilde{\mu}_p + \frac{1}{Re}\nabla^2\mathbf{v}_p + \frac{1}{\rho_p}\mathbf{F}, \quad (3)$$

$$\frac{d\mathbf{v}_n}{dt} + (\mathbf{v}_n \cdot \nabla)\mathbf{v}_n = -\nabla\tilde{\mu}_n - \frac{1}{\rho_n}\mathbf{F}, \quad (4)$$

$$\nabla \cdot \mathbf{v}_p = \nabla \cdot \mathbf{v}_n = 0, \quad (5)$$

where ρ_p and ρ_n are the relative densities of protons and neutrons (normalised so that $\rho_p + \rho_n = 1$), and Re is the Reynolds number. The mutual friction force, \mathbf{F} , is a term that describes the interaction between the proton and neutron fluids, which arises primarily from the scattering of electrons off vortex cores (Alpar, Langer & Sauls 1984). It is a combination of the Magnus and drag forces of the form (Hall & Vinen 1956)

$$\mathbf{F} = \rho_n B \hat{\boldsymbol{\omega}} \times (\boldsymbol{\omega} \times \mathbf{v}_{pn}) + \rho_n B' \boldsymbol{\omega} \times \mathbf{v}_{pn}, \quad (6)$$

where $\boldsymbol{\omega} = \nabla \times \mathbf{v}_n$ is the superfluid vorticity, $\hat{\boldsymbol{\omega}}$ is the vorticity unit vector and $\mathbf{v}_{pn} = \mathbf{v}_p - \mathbf{v}_n$ is the velocity lag between the two fluids, written as $v_i^{yx} = v_i^y - v_i^x$ in equation (2). The parameters B and B' are related ($B' \approx B^2$) dimensionless constants (Andersson, Sidery & Comer 2006). Vortex lines have a tendency to resist bending, which results in a tension

¹ By neglecting the entrainment and all viscous terms but the shear viscosity of the ‘normal’ fluid, the second-rank tensor equation (2) is reduced to a vector equation. From here on, all equations are written using conventional vector notation.

force which can be included in (6) (Hills & Roberts 1977; van Eysden 2015). For simplicity, we ignore the effect of vortex tension, c.f. Peralta et al. (2008). We also neglect vortex tangles and their effect on (6) (Gorter & Mellink 1949; Peralta et al. 2006; Andersson, Sidery & Comer 2007).

Equations (3)–(5), although derived to describe a condensate coupled to a viscous fluid in a neutron star, are formally identical to the Hall-Vinen-Bekarevich-Khalatnikov (HVBK) equations generally used to describe a (laboratory) condensate coupled to its thermal excitations (Hall & Vinen 1956; Chandler & Baym 1986), thus allowing us to make use of numerical schemes developed for the HVBK formalism (Henderson & Barenghi 1995; Peralta et al. 2008). In this context we note that the superfluid pairing gaps are density dependent in a neutron star, so there may be regions in which the superfluid transition temperature is small, and thermal excitations are important. In the present analysis, given the many other simplifying assumptions, we neglect this effect.

3 NUMERICAL METHOD

3.1 Pseudospectral solver

To solve the equations of motion (3)–(5), a pseudospectral collocation method is used to discretize the spatial coordinates, and a fractional timestep algorithm is used to advance the solution in time (Canuto et al. 1993). An explicit algorithm (third-order Adams-Bashforth) is used to solve the nonlinear terms, while the diffusion terms are solved using an implicit Crank-Nicolson scheme to maintain numerical stability (Boyd 2013). The spectral solver is the same as that used by Peralta et al. (2005, 2008), who in turn followed Bagchi & Balachandar (2002). The radial coordinate r is expanded as a series of Chebyshev polynomials, and the angular coordinates θ and ϕ are expanded as Fourier series with parity correction at the coordinate singularity at the poles. For a detailed description of the solver, see section 3 and the appendix of Peralta et al. (2008). The computational domain and boundary conditions are described in section 3.2 below. The equations of motion in this work are slightly different to those in Peralta et al. (2005, 2008), as noted in section 2.

3.2 Initial and boundary conditions

We solve equations (3)–(5) within a spherical Couette geometry, consisting of two concentric spherical boundaries rotating about a common axis. Figure 1 shows a schematic of the computational domain. The inner sphere radius is R_1 , the outer sphere radius is R_2 , and the respective angular speeds are Ω_1 and Ω_2 . In spherical coordinates the computational domain is

$$R_1 \leq r \leq R_2 \quad (7)$$

$$-\pi/2 \leq \theta \leq \pi/2 \quad (8)$$

$$0 \leq \phi \leq 2\pi. \quad (9)$$

The domain is discretised in space according to a Gauss-Lobatto quadrature scheme [Canuto et al. (1993); also see Appendix A of Peralta et al. (2008)], and we typically have $N_r \times N_\theta \times N_\phi = 121 \times 120 \times 4$ discretisation points. The coarse

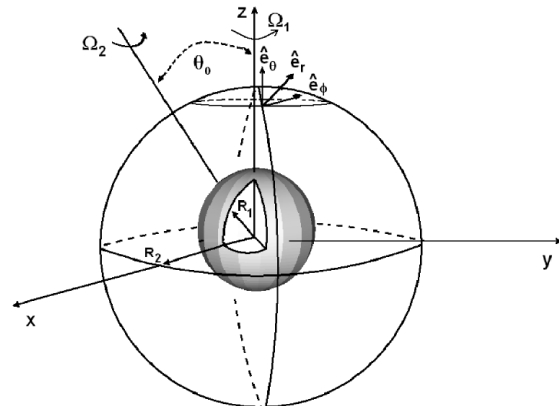


Figure 1. Illustration of the model neutron star’s geometry. A spherical surface of radius R_1 is embedded inside a larger spherical surface of radius R_2 with the same origin. Both spheres may rotate about independent axes, with respective angular velocity vectors Ω_1 and Ω_2 , though in this paper we only consider rotation about a common axis. The Cartesian coordinates are defined so that the inner sphere rotates around the z axis, and the orthonormal vectors $\hat{e}_{r,\theta,\phi}$ form the basis of the spherical coordinate system. Taken from Peralta (2006).

discretisation in ϕ is appropriate, since the common rotation axis of the crust and core prevents non-axisymmetric flow states, a result which was verified in Peralta et al. (2005, 2008).

In what follows, we express all variables in dimensionless form. We normalize times with respect to $\Omega_1(t=0)^{-1}$, so that one rotation period at $\Omega_1(t=0)$ corresponds to 2π time units. Lengths are normalized with respect to R_1 , and velocities with respect to $R_1\Omega_1(t=0)^{-1}$. The mass normalization, which affects quantities like the density, moment of inertia, and torque, is discussed below equation (13) in section 4.1.

A spherical Couette geometry is adopted primarily for numerical reasons, i.e. to avoid the coordinate singularity at $r=0$ and stabilize the evolution; flows with $R_2 - R_1 \geq 0.5R_1$ are notoriously unstable (Benton & Clark Jr 1974; Yavorskaya et al. 1980; Nakabayashi, Zheng & Tsuchida 2002). The geometry is justified physically as an idealized model of either the outer core region of a neutron star, in which case the outer boundary is the crust/core interface, or the inner crust region, in which case the outer boundary is the neutron drip point. In either case the inner boundary represents some phase separatrix, below which the fluids are more tightly coupled by (say) a rapid increase in the strength of mutual friction with decreasing radius (Alpar, Langer & Sauls 1984). Nonetheless, the presence of a rigid inner boundary is an artificial constraint in our model system. In our simulations we typically set the dimensionless gap width to be $\delta = (R_2 - R_1)/R_1 = 0.2$. The region between R_1 and R_2 is filled with a two-component fluid with component densities $\rho_p = \rho_n = 0.5$ and a Reynolds number of $Re = 500$ for the proton fluid. Both of these numbers are artificial, most estimates suggest $\rho_n \approx 0.9$ (Lattimer & Prakash 2004), and Re may be as high as 10^{11} (Mastrano & Melatos 2005; Melatos & Peralta 2007), but these values are chosen for numerical reasons.

At $t=0$, the inner and outer boundaries are corotating

at $\Omega(t=0) = 1$. The simulation runs in a reference frame rotating at $\Omega_f = \Omega(t=0)$ for all t , which introduces Coriolis terms, $2\mathbf{\Omega}(t=0) \times \mathbf{v}_{p,n}$, on the right-hand sides of equations (3) and (4). The initial conditions imply $\mathbf{v}_p = \mathbf{v}_n = 0$ everywhere at $t = 0$.

For both the proton and neutron velocity fields, we impose no-penetration and no-slip boundary conditions. Mathematically, these boundary conditions can be expressed as

$$\mathbf{v}_{p,n}(R_{1,2}, \theta, \phi) = R_{1,2}\mathbf{\Omega}_{1,2} \times \hat{\mathbf{r}}, \quad (10)$$

where $\mathbf{\Omega}_{1,2}$ is the angular velocity of the boundary, and $\hat{\mathbf{r}}$ is the radial unit vector. The use of these boundary conditions is motivated primarily by numerical considerations. However, there is some physical justification as well. At $r = R_2$, no-penetration reflects the inability of either fluid to flow through the solid crust. No-penetration at $r = R_1$ is more artificial. Viscous processes as well as magnetic coupling keep the proton fluid near both boundaries in corotation, implying no-slip for \mathbf{v}_p . The boundary condition for the superfluid neutrons depends on the interaction between individual vortex lines and the surface. Following Khalatnikov & Hohenberg (1965), the relative motion between a vortex line with tangential velocity \mathbf{v}_L and a boundary moving with velocity \mathbf{u} can be written as

$$\mathbf{v}_L - \mathbf{u} = c_1 \hat{\mathbf{\omega}}_n \times (\mathbf{n} \times \hat{\mathbf{\omega}}_s) + c_2 \mathbf{n} \times \hat{\mathbf{\omega}}_n, \quad (11)$$

where \mathbf{n} is the unit normal to the boundary. The coefficients $c_{1,2}$ parametrize the amount of slip. The two extremal cases are perfect sliding ($c_1 = c_2 \rightarrow \infty$) and no-slip ($c_1 = c_2 = 0$). One is usually obliged to set c_1 and c_2 on empirical grounds, even for well-studied and controlled situations involving liquid helium, let alone under the uncertain conditions present in a neutron star. Peralta et al. (2005, 2008) investigated boundary conditions extensively with this solver and encountered numerical difficulties for choices other than no-slip [c.f. Reisenegger (1993) and van Eysden (2015) for a discussion of alternatives in analytic calculations]. As mentioned above, we consider the viscous and inviscid components to be locked together for $r < R_1$ and postulate that the fluid immediately adjacent to this region is also strongly coupled, i.e. $c_1 = c_2 = 0$ at $r = R_1$.

3.3 Model assumptions and limitations

Necessarily, the above model involves several simplifying assumptions. Some of these stem from a lack of theoretical consensus about aspects of the physics, while others are made in order to make a difficult numerical problem more tractable. We introduce the assumptions as they arise in previous sections. Here we summarize them together and discuss why they have been made, how they affect the applicability of our results to real pulsars, and how future work might refine the model.

- *Equations of motion.* The incompressibility condition (5) is justified, because the sound speed in a neutron star is much greater than the flow speeds. By contrast, the assumption of constant, uniform density does break down in the outer core modelled here. Work is currently under way to adapt the Navier-Stokes solver on which our two-fluid solver is based to work with non-uniform densities (K. Poon, private communication, 2015). The absence of entrainment is

valid as long as the simulation volume represents the outer core, where entrainment is weak (Carter, Chamel & Haensel 2006). However, the inclusion of an entrainment term in equations (3) and (4) is relatively straightforward and represents a promising direction for future work. Vortex tension is another effect we have neglected. van Eysden & Melatos (2013) showed that in the crust of a neutron star the effect of vortex tension is small and confined to a boundary layer, though more recent work (van Eysden 2015) suggests that vortex tension adds an oscillatory component to glitch recovery. As with entrainment, it is relatively straightforward to include vortex tension in the solver as a natural next step.

- *Spherical Couette geometry and boundary conditions.* In section 3.2 we explain the reasons for using a spherical Couette geometry with no-slip boundaries at R_1 and R_2 . This is an obvious limitation, as it restricts the model to a specific region of the star and imposes an artificial boundary condition at the inner boundary, yet it is unavoidable: the solver in its present form (section 3.1) is unstable numerically when applied to a complete sphere. The appropriate boundary conditions for a superfluid in a rotating spherical container remain unclear and depend on the configuration of the vortex array and its interaction with the boundary (Khalatnikov & Hohenberg 1965; Henderson, Barenghi & Jones 1995; Peralta et al. 2008). Theoretical work by Campbell & Krasnov (1982) suggests that the vortex-boundary interaction is important in a spin-down context, as the rate of vortex nucleation is greater for rough boundaries than for smooth boundaries, so a rough boundary may decrease spin-down rate of the condensate. Future laboratory experiments with superfluid helium may shed some light on appropriate boundary conditions, but there is no guarantee that the results of such an experiment would be applicable to a fermion condensate in a neutron star. Experiments with liquid helium demonstrate that vorticity is transported erratically instead of smoothly across a two-phase boundary, such as at $r = R_1$, in response to interfacial Kelvin-Helmholtz instabilities, an effect which we do not include (Blaauwgeers et al. 2002; Mastrano & Melatos 2005). The use of a solid boundary at R_2 is also unphysical, because the crust-core interface is not sharply delineated, and the solid and superfluid components interact non-trivially through magnetic and elastic coupling. Andersson, Haskell & Samuelsson (2011) developed a hydrodynamic formalism for investigating the crust-core coupling, which may be useful in the future for determining appropriate boundary conditions in an astrophysical context. Numerical studies of vortex motion are another avenue through which this issue might be investigated in the future (Schwarz 1985; Adachi, Fujiyama & Tsubota 2010; Baggaley & Barenghi 2012).

- *Astrophysical parameters.* Certain parameters of the model are poorly constrained, because bulk nuclear matter in the low-temperature, high-density regime of neutron stars cannot be studied easily in laboratory experiments. For example, the relative moments of inertia of the crust and the superfluid depend on the precise equation of state for bulk nuclear matter, and inferred values from measurements of pulsar glitches only weakly constrain these (sections 4.1 and 6.2). Where possible we use the best current estimates and cite relevant literature, e.g. the values of the mutual friction parameters B and B' (section 2). In other places, we use artificial values for numerical stability or for illustrative

purposes, all of which are explained in the relevant sections, e.g. the value of Re (section 4.1). Future work will explore the parameter space more widely, in preparation for new observational studies of pulsar glitches and gravitational waves (Weber et al. 2007; van Eysden & Melatos 2010).

4 STEADY PRE-GLITCH SPIN DOWN

Before investigating the post-glitch response in section 5, we discuss how to set up the simulation to achieve a realistic initial state leading up to the glitch.

4.1 Set up

Many models of glitches posit that, as a neutron star spins down, the deceleration of the condensate lags that of the viscous component and the crust, due to vortex pinning. As the lag builds up, the pinned vortices act as a reservoir of angular momentum, which can recouple with the viscous fluid and crust spasmodically, causing glitches (Anderson & Itoh 1975; Warszawski & Melatos 2011; Haskell & Melatos 2015). To simulate glitches in this paradigm, we need to prepare the system in a state where there is a lag between the neutron and proton velocities prior to a glitch. There is no analytic solution for high-Reynolds-number spherical Couette flow in such a state. Instead, we begin with the inner and outer boundaries corotating and spin down the outer sphere by imposing an external torque, analogous to the star’s electromagnetic braking torque (Melatos 1997). As the external torque spins down the outer boundary, the neutron and proton fluids near the no-slip boundary also spin down, and the deceleration is communicated to the interior by Ekman pumping (Melatos 2012; van Eysden & Melatos 2014; van Eysden 2015).

In response to the external torque, opposing viscous torques N_1 and N_2 are induced by the gradients of \mathbf{v}_p at $r = R_1$ and R_2 (Landau & Lifshitz 1959). At each time step, the viscous torque is calculated by integrating the non-vanishing terms of the stress tensor over the surfaces $r = R_1, R_2$. Assuming axisymmetric flow one finds

$$N_{1,2} = \frac{2\pi R_{1,2}}{Re} \int d\theta \sin \theta \left(\left. \frac{\partial v_p^\phi}{\partial r} \right|_{r=R_{1,2}} - \frac{v_p^\phi}{R_{1,2}} \right). \quad (12)$$

The angular velocities of the boundaries, $\Omega_{1,2}$, evolve according to

$$I_{1,2} \frac{d\Omega_{1,2}}{dt} = N_{1,2} + N_{\text{ext}}, \quad (13)$$

where I_1 and I_2 are the moments of inertia of the inner core and the crust, and N_{ext} is the external torque. Equation (13) is solved at each timestep using a third-order Adams-Bashforth algorithm, so as to maintain the same time-accuracy as the pseudospectral solver. The moment of inertia is expressed in dimensionless units, normalized with respect to $(\rho_p + \rho_n)R_1^5$. This means that the moment of inertia of the fluid in the interior, notionally regarded as a rigid body, is $I_3 = 2.5$. We choose the moment of inertia of the crust, I_2 so that $I_2/I_3 = 4$, and the moment of inertia of the core, I_1 , to satisfy $I_2/I_3 = 4$ and $I_1/I_2 = 10$. These numbers give the fractional moment of inertia due to the condensate as 1.1%, which is similar to the value of this

ratio in glitching pulsars (Link, Epstein & Lattimer 1999; Andersson et al. 2012). The external torque, N_{ext} is chosen so that a decoupled crust with moment of inertia I_2 decelerates at $\dot{\Omega} = N_{\text{ext}}/I_2 = -10^{-3}$. This is artificially high; most pulsars have $|\dot{\Omega}| \sim 10^{-15}$ (Manchester et al. 2005). However, it is necessary so that an appreciable lag builds up between the crust and other components in the duration of a typical simulation.

Three important time-scales in this system are the viscous time-scale, $\tau_{\text{visc}} = Re/\Omega$, the Ekman time-scale, $\tau_{\text{Ek}} = \sqrt{Re}/\Omega$, and the mutual friction time-scale, $\tau_{\text{MF}} = 1/(2\Omega B)$. In a neutron star, we are interested in two regimes: the viscous-dominant regime, $\tau_{\text{Ek}} < \tau_{\text{visc}} < \tau_{\text{MF}}$, and the mutual friction-dominant regime, $\tau_{\text{MF}} < \tau_{\text{Ek}} < \tau_{\text{visc}}$, which we refer to as weak and strong mutual friction respectively for the remainder of this paper. For the strong mutual friction case, we take $B = 0.1$, and for weak mutual friction we have $B = 10^{-4}$, which are typical values for Kelvin wave damping and electron scattering respectively (Alpar, Langer & Sauls 1984; Andersson, Sidery & Comer 2006; Haskell, Pizzochero & Sidery 2012). We typically have $Re = 500$, which is significantly lower than realistic neutron star values of $Re \sim 10^{11}$ (Mastrano & Melatos 2005; Melatos & Peralta 2007). In the interest of computational tractability we choose lower values of Re to avoid turbulence in the viscous component (Peralta et al. 2005), which would require increased spatial resolution, and to reduce the important time-scales τ_{Ek} and τ_{visc} .

Starting from a state of corotation, we impose a constant torque on the outer boundary and evolve the system until the inner and outer boundaries are spinning down at approximately the same rate, i.e. we have $\dot{\Omega}_1 \approx \dot{\Omega}_2$. We refer to this state as ‘spin-down equilibrium’ and use it as a starting point for our simulations of glitches. Note that $\dot{\Omega}_1 \approx \dot{\Omega}_2$ does not imply $\dot{\mathbf{v}}_{pn} \approx 0$. The majority of the angular momentum in the model pulsar is in the heaviest region, $r < R_1$, which couples to the crust and proton fluid on either the viscous or Ekman timescales (van Eysden & Melatos 2014). To reach spin-down equilibrium, we need $t > \tau_{\text{visc}} > \tau_{\text{Ek}}$, however, it is still possible for the lag between the proton and neutron fluids to grow, as the maximum value of \mathbf{v}_{pn} is determined by mutual friction, and is not reached until we have $t > \tau_{\text{MF}}$. Evolving the system until one has $\dot{\mathbf{v}}_{pn} = 0$ may seem a more natural initial condition for a glitch, but in practice τ_{MF} can be prohibitively long for numerical experiments. Moreover, it is unclear whether neutron stars ever reach such a state in reality, as the glitch trigger mechanism is unknown, hydrodynamical instabilities could set in long before the velocity lag reaches equilibrium (Andersson, Comer & Prix 2004), and stratification acts to maintain a shear (Melatos 2012). Similar issues arise in laboratory experiments with liquid helium (van Eysden & Melatos 2011).

4.2 Output and initial state

Figure 2 shows the evolution of $\Omega_1(t)$, $\Omega_2(t)$, $\dot{\Omega}_1(t)$, and $\dot{\Omega}_2(t)$, for $0 \leq t \leq 500$. From the bottom two panels, we can see that the system reaches steady deceleration by $t = 500$: we obtain $\dot{\Omega}_1 \approx \dot{\Omega}_2 \approx -9.5 \times 10^{-5}$, and $|\dot{\Omega}_1 - \dot{\Omega}_2|/|\dot{\Omega}_1| \lesssim 5\%$, and the angular velocity lag between the crust and core

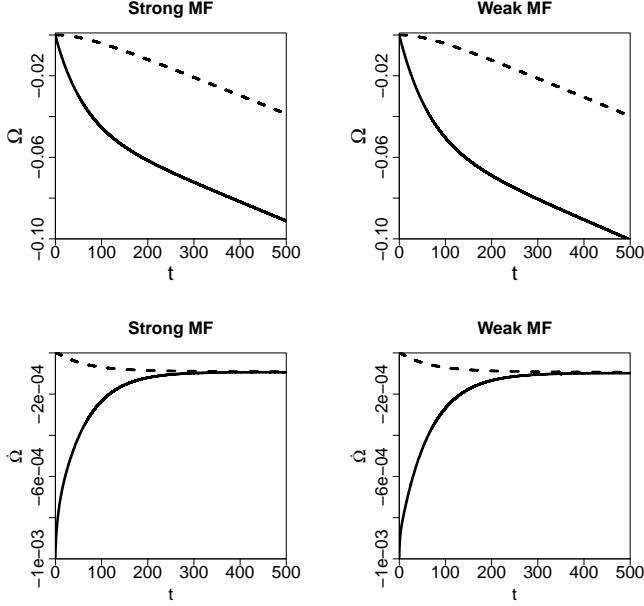


Figure 2. Response of the crust and core spin frequencies, $\Omega_1(t)$ and $\Omega_2(t)$, and their time derivatives, $\dot{\Omega}_1(t)$, and $\dot{\Omega}_2(t)$, to a constant external torque on the crust, for $0 \leq t \leq 500$, with strong (left column) and weak (right column) mutual friction, with $\Omega_1(t=0) = \Omega_2(t=0)$. In this figure, Ω_1 and Ω_2 are measured in a frame rotating with angular velocity $\Omega_f = \Omega_1(t=0) = \Omega_2(t=0)$ and are also normalized with respect to Ω_f . Time is normalized with respect to Ω_f^{-1} . The top row is the crust spin frequency, $\Omega_1(t)$, (dashed curves), and the core spin frequency, $\Omega_2(t)$, (solid curves). The bottom row is the crust frequency derivative, $\dot{\Omega}_1(t)$, (dashed curves), and the core frequency derivative $\dot{\Omega}_2(t)$, (solid curves). In both mutual friction regimes the two boundaries are decelerating at approximately the same rate after $t = 500$, a state we refer to as spin-down equilibrium.

$\Omega_2(t=500) - \Omega_1(t=500)$ is -0.52 with strong mutual friction and -0.61 with weak mutual friction.

The deceleration is faster with weak mutual friction, as shown in the top two panels. This is because the neutron and proton components couple only after $t > \tau_{MF} = 500$ (weak), so for $t < 500$ the external torque is only spinning down the viscous component, the core and the crust. With strong mutual friction, the inviscid component couples to the viscous component after $t > \tau_{MF} = 5$ (strong), so the moment of inertia of the coupled system is greater than with weak mutual friction, and the magnitude of its deceleration is reduced.

For a more detailed view of the flow, we look in figure 3 at contours of v_{pn}^ϕ in the strong mutual friction regime in a slice through the y - z plane, at $t = 5 \approx \tau_{MF} < \tau_{Ek} \ll \tau_{visc}$. It is clear that the flow is axisymmetric but not columnar; the contours of v_{pn}^ϕ are curved. An expanded view of the flow in the top-right quadrant of the y - z plane appears in Figure 4, at $t = 5, 25, 100$, and 500 . The contours in the remainder of the domain can be inferred from the symmetries in Figure 3. For strong mutual friction (left column), there is a noticeable difference between the flow at $t = 5$ (top row) and at later times. At $t = 5$, v_{pn}^ϕ has a maximum at $r \approx R_2$, at a latitude of $\theta \approx 30^\circ$. At fixed radius, v_{pn}^ϕ decreases slowly with latitude: $v_{pn}^\phi(r \approx R_2, \theta = 0) \approx 0.75v_{pn,\max}^\phi$. For $t \geq 25$

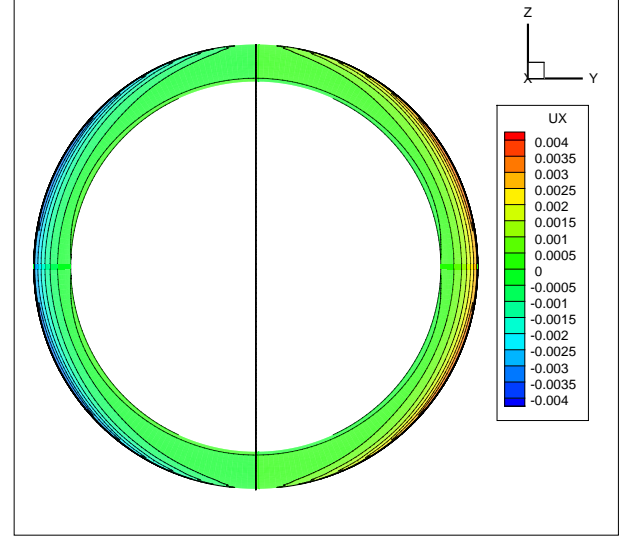


Figure 3. Contours of the azimuthal velocity lag, v_{pn}^ϕ , plotted at $t = 5 \approx \tau_{MF} < \tau_{Ek} < \tau_{visc}$ in the y - z plane, with strong mutual friction. Velocity is expressed in dimensionless units normalized with respect to $R_1\Omega_f^{-1}$. v_{pn}^ϕ is non-zero near $r = R_2$, but decreases monotonically to zero as $r \rightarrow R_1$. $|v_{pn}^\phi|$ increases from zero at the poles to a maximum at $\theta \approx 30^\circ$ in latitude. The flow is axisymmetric but not columnar, as the 18 contours have similar curvature to the boundaries throughout most of the domain.

(second row and below), $v_{pn,\max}^\phi$ is still near $r = R_2$ and $\theta = 30^\circ$, however, v_{pn}^ϕ falls off more steeply with decreasing latitude, with $v_{pn}^\phi(r \approx R_2, \theta = 0) \approx 0.25v_{pn,\max}^\phi$ at $t = 25$ and $\approx 0.1v_{pn,\max}^\phi$ at $t = 500$. For weak mutual friction, the flow pattern does not change significantly between $t = 5$ and $t = 100$, apart from a steady increase in $|v_{pn}^\phi|$. Another notable difference between the two regimes is that v_{pn}^ϕ decreases monotonically from $v_{pn,\max}^\phi$ at $r = R_2$ to zero at $r = R_1$ for weak mutual friction, while it decreases to $-v_{pn,\max}^\phi$ at $r = R_1$ for strong mutual friction. To investigate the sign-reversal of v_{pn}^ϕ more closely, we first average v_{pn}^ϕ over the angular coordinates, θ and ϕ , and examine the radial profile of the averaged velocity, $\langle v_{pn}^\phi \rangle_{\theta,\phi}$, in figure 5. At $r = R_1$ and R_2 , the two fluids are locked together by the no-slip boundary condition.

Away from the boundaries, an interesting feature develops with strong mutual friction: $\langle v_{pn}^\phi \rangle_{\theta,\phi}$ undergoes a sign change. Naïvely, one expects the inviscid neutron condensate to lag the protons, because Ekman pumping acts on the protons to bring them into corotation with the boundaries after $t \approx \tau_{Ek}$, while there is no equivalent process for the condensate. When mutual friction is weak, this is indeed the case. For $\tau_{MF} < \tau_{Ek}$, however, the protons drag the neutrons along as Ekman pumping proceeds. Equations (3) and (4) differ in form, so different flow patterns develop in the two components [van Eysden & Melatos (2013); in particular see Figures 1 – 6 in the latter paper]. In Figure 6, we show the streamlines of the protons (top) and neutrons (bottom) at $t = 500$ with strong mutual friction. It is clear that the flow states are distinct. For the proton component, the meridional circulation is centred at $\theta \approx 30^\circ$ at $r \approx 0.5(R_1 + R_2)$. The streamlines are parallel to the boundaries at $r \approx R_1$ and $r \approx R_2$ and elsewhere they bend

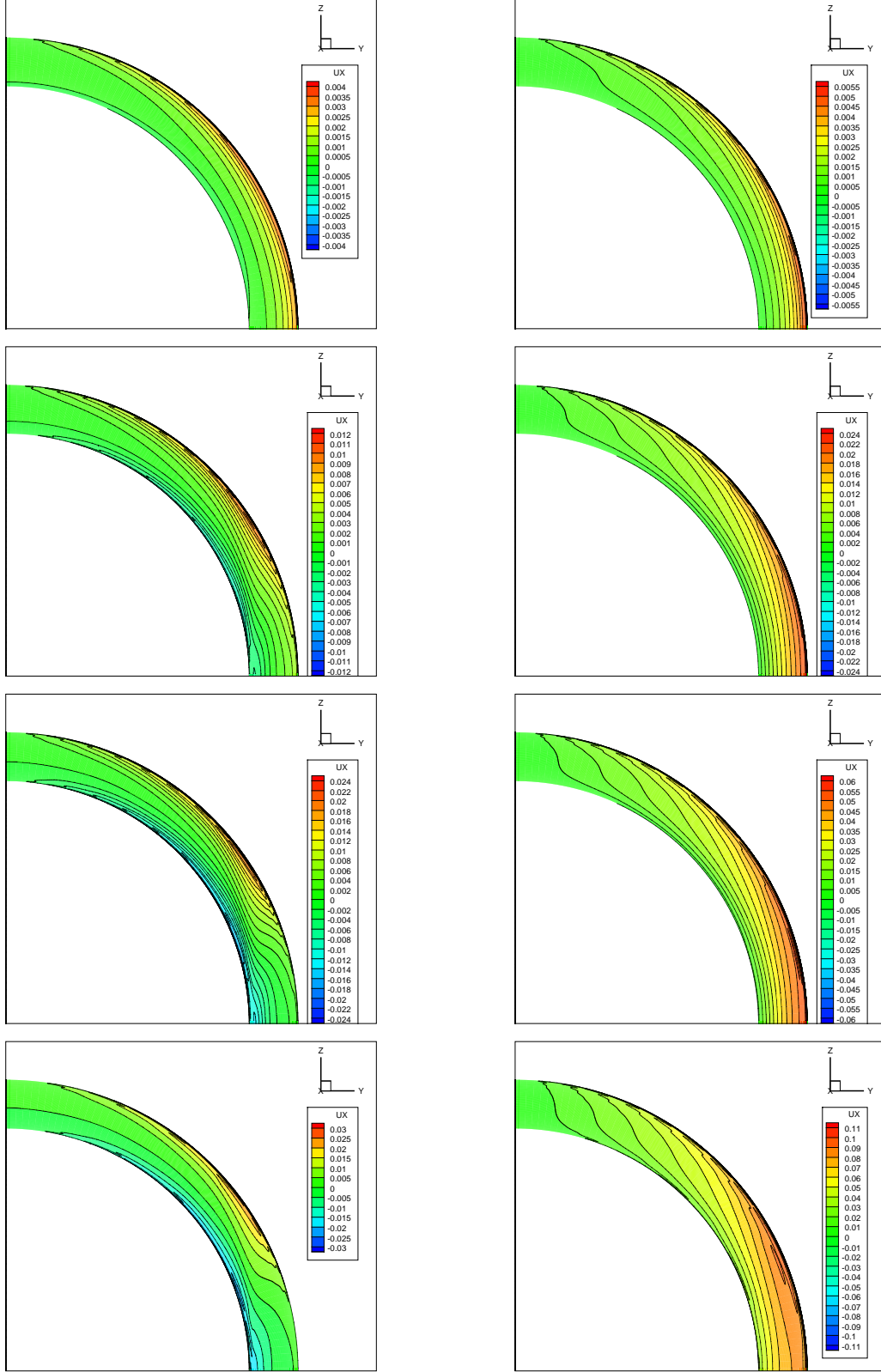


Figure 4. Contours of the azimuthal component of the proton-neutron velocity lag, v_{pn}^ϕ , in the meridional plane, for strong mutual friction (left column), and weak mutual friction (right column), at $t = 5, 25, 100$, and 500 (top to bottom row respectively). Velocity is expressed in dimensionless units normalized with respect to $R_1 \Omega_f^{-1}$. Red colours show positive lag into the page, blue colours show lag out of the page. Rotation is about the positive z -axis. Early on both mutual friction regimes exhibit similar flow patterns: The value of v_{pn}^ϕ is highest near the outer boundary, having its maximum value $\theta \approx \pm 30^\circ$ in latitude. Later on, for strong mutual friction, the region where v_{pn}^ϕ is maximised migrates away from the equator, and v_{pn}^ϕ changes sign between the inner and outer boundaries.

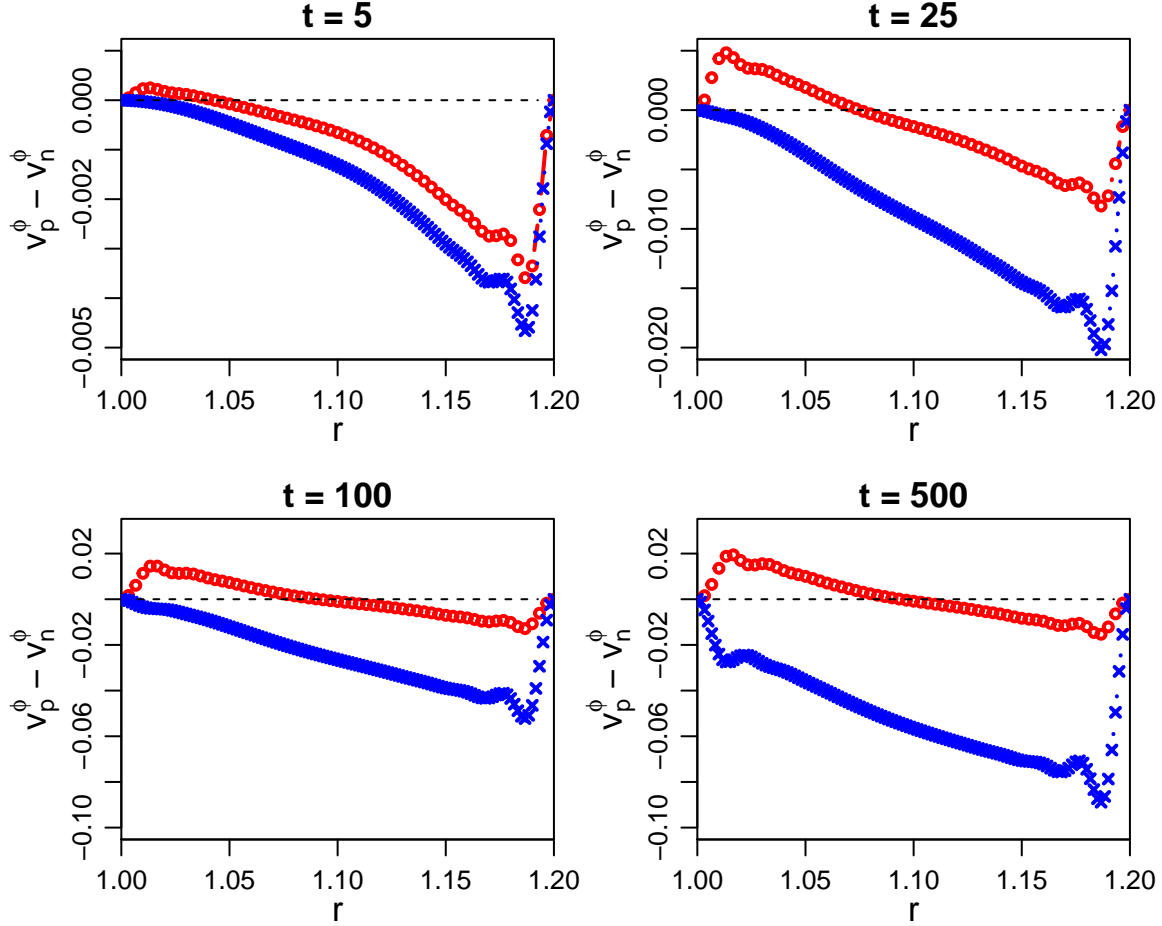


Figure 5. Snapshots of the θ and ϕ -averaged azimuthal velocity lag, $\langle v_{\text{pn}}^\phi \rangle_{\theta, \phi}$, versus cylindrical radius r , at $t = 5$ (top left), 25 (top right), 100 (bottom left), and 500 (bottom right). Time is expressed in dimensionless units normalized with respect to the angular velocity of the rotating frame Ω_f^{-1} , and velocity is expressed in dimensionless units normalized with respect to $R_1 \Omega_f^{-1}$. The red curve (circles) and the blue curve (crosses) correspond to strong and weak mutual friction respectively. The boundary condition enforces $v_{\text{pn}}^\phi = 0$ at $r = R_1$ and $r = R_2$. When mutual friction is strong, v_{pn}^ϕ changes sign near $r = R_1$. When mutual friction is weak, the viscous component spins down faster than the condensate throughout the domain.

inwards. For the neutron component, the streamlines are less symmetric. The primary cell is centered at $\theta \approx 20^\circ$ and is closer to $r = R_1$ than $r = R_2$. The flow is roughly columnar, with a Stewartson layer partially forming at $r \sin \theta \approx R_1$ (Peralta & Melatos 2009). Subtracting the flow patterns in the two panels of Figure 6 (see bottom left panel of Figure 4), we find that the neutrons spin down faster than the protons at $r \approx R_1$.

5 POST-GLITCH RECOVERY

5.1 Activating the glitch

We simulate glitches by taking, as initial conditions, the velocity fields and boundary conditions of the system after 500 time units of steady spin down and modifying them impulsively in one of three ways. Firstly, we spin up the outer boundary instantaneously, which we call a ‘crust glitch’. Secondly, we recouple the proton and neutron fluids instantaneously, so that v_{pn}^ϕ is reduced to zero everywhere in a step,

which we call a ‘bulk glitch’. Thirdly, we spin up the core instantaneously, which we call an ‘inner glitch’.

We can think of a crust glitch as the response to a crustquake, caused by shear stresses (Ruderman 1969; Middleton et al. 2006), or crust cracking due to a build-up of superfluid vortices at the crust (Alpar et al. 1996). Similarly, inner glitches represent a violent event occurring within the core, at $r < R_1$, e.g. an avalanche of superfluid vortices pinned to magnetic flux tubes (Link 2012). Some models of core matter, such as color superconducting condensates, predict a high shear modulus (Mannarelli, Rajagopal & Sharma 2007) so that seismic disturbances (‘corequakes’) may have observable effects on the crust (Ruderman 1976; Ruderman, Zhu & Chen 1998).

Bulk glitches correspond to trigger mechanisms distributed throughout the superfluid itself, in the region $R_1 \leq r \leq R_2$. When $|\mathbf{v}_{\text{pn}}|$ grows too large, a hydrodynamical instability similar to the two-stream instability can occur, which acts to reduce the velocity lag between the two components (Andersson, Comer & Prix 2004; Mastrano & Melatos

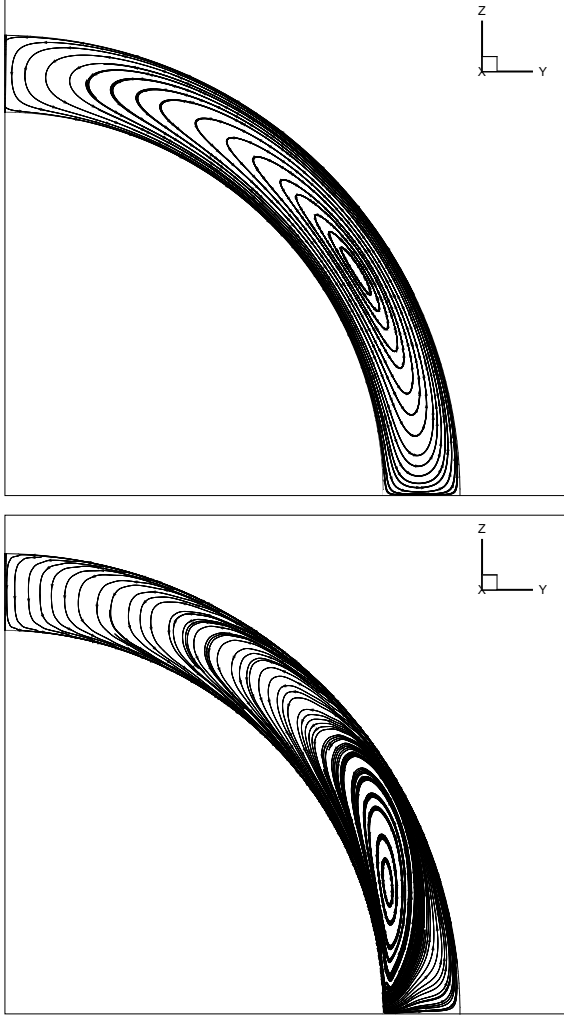


Figure 6. In-plane meridional streamlines of the protons (top) and neutrons (bottom) with strong mutual friction at $t = 500$. Both components show meridional circulation, but the flows are distinct. In the protons the circulation is centered at $\theta \approx 30^\circ$ and $r \approx 0.5(R_1 + R_2)$, while for the neutrons the circulation cells are centered at $\theta \approx 20^\circ$ and $r \approx R_1$. This difference in flow patterns leads to the result shown in Figure 4, where v_{pn}^ϕ changes sign in the region $R_1 < r < R_2$ for strong mutual friction.

2005; Glampedakis & Andersson 2009). Another potential trigger is a vortex avalanche, driven by the shear between the bulk fluid and pinned vortices (Warszawski, Melatos & Berloff 2012).

Following a glitch, we evolve the system for a further 500 time units. We also run a control simulation, where steady spindown continues uninterrupted for a further 500 time units, i.e. no glitch. We compare $\Omega_2(t)$ with and without a glitch and construct ‘residuals’ $\Delta\Omega(t) = \Omega_{2,g}(t) - \Omega_{2,ng}(t)$, where $\Omega_{2,g}(t)$ and $\Omega_{2,ng}(t)$ are the values of Ω_2 with and without a glitch respectively. The residual has two advantages. First, in reality, glitches are detected as deviations in pulse times-of-arrival from a non-glitch spin-down model (Hobbs, Edwards & Manchester 2006; Espinoza et al. 2011). Second, the residuals separate the glitch evolution from that due to the external torque, which remains constant throughout the post-glitch simulation (the glitch recovery time-scale

is much shorter than the spin-down time-scale). Note that $\Omega_1(t)$ also evolves, consistent with equation (13).

5.2 Fitting the glitches

Generally, pulsar glitches are followed by a recovery phase, during which some or all of the increase in spin frequency is reversed. It is common to fit glitches to a function of the form

$$\Omega(t) = \Omega_0(t) + \Delta\Omega_p + \sum_{i=1}^N \Delta\Omega_n e^{-t/\tau_n}, \quad (14)$$

where $\Delta\Omega_p$ is the permanent change in the spin frequency and $\Delta\Omega_n$ are transient changes in the spin frequency of either sign that decay on a characteristic timescale τ_n [see e.g. Shemar & Lyne (1996); Wong, Backer & Lyne (2001)]. Further time derivatives of Ω may be included in equation (14), but are normally neglected. In section 6.1, we discuss the effect of including a permanent change in the frequency derivative, $\Delta\dot{\Omega}_p$. As many as four distinct transient timescales can be fitted for some glitches (Dodson, Lewis & McCulloch 2007), ranging from tens of seconds to hundreds of days. One-dimensional superfluid simulations in Haskell, Pizzochero & Sidery (2012) show that the recovery occurs on a combination of time-scales and is not well-approximated by a single exponential, a result which also holds for two-dimensional Ekman pumping (van Eysden & Melatos 2010). A multiple exponential fit, though, is well-motivated by theoretical work done by van Eysden & Melatos (2010, 2014), who solved analytically for the rotational evolution of a rotating vessel filled with a helium-II-like superfluid, described by the equations of motion of Chandler & Baym (1986), following an impulsive acceleration. They found that, in the limits $\tau_{\text{MF}} \ll \tau_{\text{EK}}$, $B' \ll 1$, $I_3/I_2 \gg 1$, the recovery involves two exponential timescales, which depend on the relative densities of the viscous and inviscid components, the relative strength of viscous and mutual friction forces, and the inertia of the container.

For our simulated glitches, we fit the residual $\Delta\Omega(t) = \Omega_{2,g}(t) - \Omega_{2,ng}(t)$ with five parameters: τ_1 , τ_2 , $\Delta\Omega_1$, $\Delta\Omega_2$, and $\Delta\Omega_p$. The fit is extracted using the Levenberg-Marquardt least-squares algorithm, implemented in the statistics software R with the package `minpack.lm` (Elzhov et al. 2013).

5.3 Crust glitches

To induce a crust glitch, we instantaneously increase Ω_2 by an amount $|\Omega_2 - \Omega_1|/2$ at $t = 500$. The jump is chosen arbitrarily; we find that its size does not alter the dynamics of the recovery qualitatively. Figure 7 shows the evolution of $\Delta\Omega$ following the crust glitch for strong (top panel) and weak (bottom panel) mutual friction. The parameters of the associated dual exponential fits are shown in Table 1. Immediately following the glitch $\Delta\Omega$ decreases monotonically. This happens because the no-slip boundary condition causes $v_p^\phi(r = R_2)$ to also increase, so the viscous torque, equation (12), is reduced (relative to the no-glitch simulation), and the external spin-down term in equation (13) dominates. Both strong and weak mutual friction recover similarly, with $\tau_2 \approx 64$. The fitted values of τ_1 are discrepant

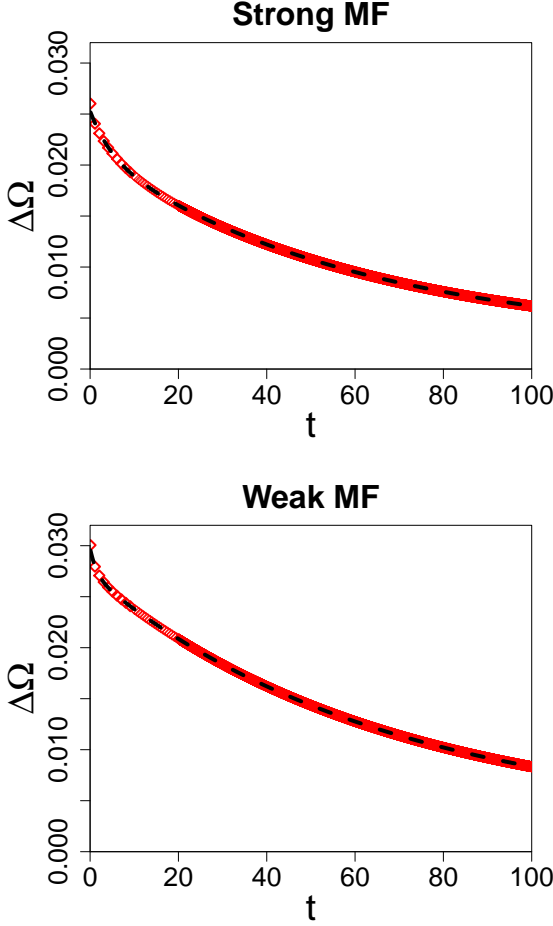


Figure 7. Angular velocity residuals, $\Delta\Omega(t) = \Omega_{2,g}(t) - \Omega_{2,ng}(t)$, for 100 time units following a crust glitch. The red diamonds show the data from the simulation. The black dashed curve shows a curve of best fit to a dual exponential recovery given by equation (14) with $N = 2$ (see Table 1 for values). Mutual friction has little effect on the recovery time-scales.

Parameter	Weak MF	Strong MF
$\Delta\Omega_1$	2.55×10^{-3}	4.15×10^{-3}
τ_1	1.53	5.15
$\Delta\Omega_2$	2.42×10^{-2}	1.86×10^{-2}
τ_2	66.4	62.0
$\Delta\Omega_p$	2.96×10^{-3}	2.46×10^{-3}

Table 1. Fitted parameters to equation (14) with $N = 2$ for the crust glitches in Figure 7 with strong ($B = 0.1$) and weak ($B = 10^{-4}$) mutual friction (MF) at $Re = 500$.

by a factor of ≈ 3 between the mutual friction regimes, however, in both cases $\Delta\Omega_1 \ll \Delta\Omega_2$, so doesn't affect the shape of the recovery profile significantly. $\Delta\Omega_p$ is $\approx 10\%$ of $\Delta\Omega_{\max}$ with strong and weak mutual friction. There is no qualitative difference between the recovery profile in the two mutual friction regimes for crust glitches. In the limits $\tau_{\text{MF}} \ll \tau_{\text{Ek}}$, $B' \ll 1$, $I_3/I_2 \gg 1$, van Eysden & Melatos (2010) derived simple analytic expressions for the time-scales of a double-

Parameter	Weak MF	Strong MF
$\Delta\Omega_1$	-4.27×10^{-3}	-2.61×10^{-4}
τ_1	1.60	0.201
$\Delta\Omega_2$	4.40×10^{-3}	2.26×10^{-4}
τ_2	68.0	59.2
$\Delta\Omega_p$	6.56×10^{-4}	1.21×10^{-6}

Table 2. Fitted parameters to equation (14) with $N = 2$ for the bulk glitches in Figure 8 with strong ($B = 0.1$) and weak ($B = 10^{-4}$) mutual friction (MF) at $Re = 500$.

exponential recovery,

$$\tau_1 \approx \tau_{\text{MF}}, \quad (15)$$

$$\tau_2 \approx \frac{\tau_{\text{Ek}}}{\rho_p(1 + I_3/I_2)} \quad (16)$$

(or vice versa). For $B = 0.1$ (strong mutual friction), equations (14) and (15) give $\tau_1 = 5$, $\tau_2 = 36$, compared to $\tau_1 = 5.15$, $\tau_2 = 62.0$ obtained from fitting to simulations. This is a decent level of agreement, though it should be noted that equations (15) and (16) are not exactly the expressions as written in van Eysden & Melatos (2010), who considered a spherical container ($R_1 = 0$) filled with a HVBK superfluid (Chandler & Baym 1986), rather than a spherical Couette geometry filled with fluid obeying equations (3) – (5). More specifically, in van Eysden & Melatos (2010), the quantity I_3/I_2 is the ratio of the moment of inertia of the interior of the sphere to that of the container, while in our analysis we exclude the moment of inertia of the core. We are also in a different parameter regime to van Eysden & Melatos (2010): we have $\tau_{\text{Ek}} \approx 5\tau_{\text{MF}}$ for strong mutual friction, and $I_3/I_2 \approx 0.25$.

5.4 Bulk glitches

To induce a bulk glitch, we instantaneously recouple the proton and neutron fluids, so that the velocity lag is reduced to zero, in a way that conserves total angular momentum. Generally, the recoupling algorithm depends on the relative moments of inertia of each fluid, but since we have $I_n = I_p$, we simply set $v_p^\phi \mapsto v_p^\phi - v_{\text{pn}}^\phi/2$, and $v_n^\phi \mapsto v_n^\phi + v_{\text{pn}}^\phi/2$. Figure 8 displays the residual $\Delta\Omega$ in the 100 time units of simulation time following a bulk glitch with strong and weak mutual friction. The recovery is fitted to equation (14), and the fitted parameters are quoted in Table 2.

For both strong and weak mutual friction, the crust spins up immediately after recoupling. Unlike crust glitches, where the spin up is instantaneous by construction, there is a noticeable rise time in $\Delta\Omega$, which is reflected in the fitting algorithm returning $\Delta\Omega_1 < 0$ in Table 2. The reason that $\Delta\Omega$ increases initially is that spinning up the protons increases $\partial v_p^\phi / \partial r|_{r=R_2}$, N_2 [via equation (12)], and hence $\Delta\Omega$ [via equation (13)]. As the crust spins up, however, the no-slip boundary condition increases $v_p^\phi(r = R_2)$, which acts to reduce the viscous torque and halt the spin up after $t \approx 5$. $\Delta\Omega$ reaches a maximum at similar times for both strong and weak mutual friction regimes ($t = 5.0$ and $t = 6.3$ respectively), which corresponds to approximately one rotation period of the star $P = 2\pi/\Omega_2 = 7.0$. The spin up time is also similar to τ_{MF} for strong mutual friction, as discussed further in

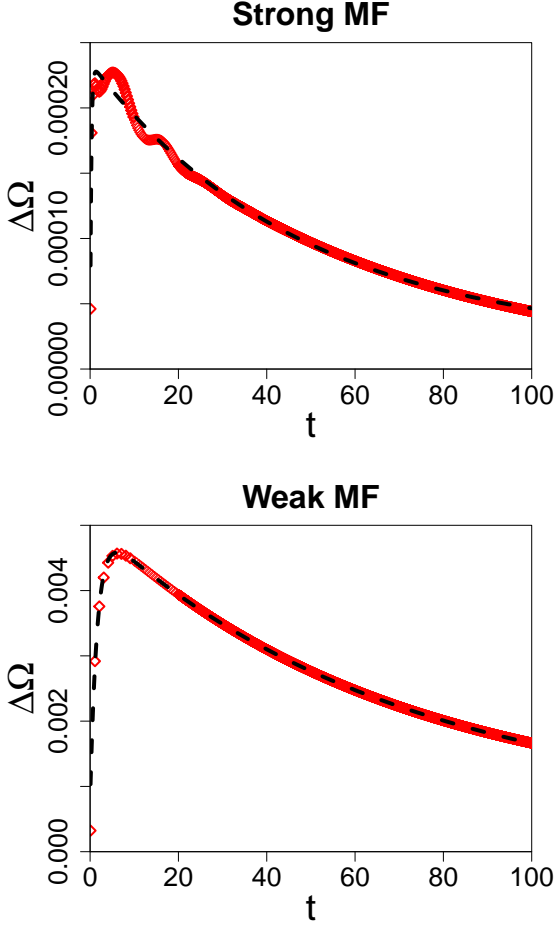


Figure 8. Angular velocity residuals, $\Delta\Omega(t) = \Omega_{2,g}(t) - \Omega_{2,ng}(t)$, for 100 time units following a bulk glitch. The red diamonds show the data from the simulation. The black dashed curve shows a curve of best fit to a dual exponential recovery given by equation (14) with $N = 2$ (see Table 2 for values). With strong mutual friction, the size of the glitch is significantly reduced, and there is an oscillatory component to the recovery for $t \lesssim 30$.

section 6.2. For $t \gtrsim 5$, $\Delta\Omega$ decreases on a time-scale of $\tau_2 \approx 65$. This is because the spin up of the crust following the glitch reduces the angular velocity lag between the crust and core and upsets spin-down equilibrium. In order to restore spin-down equilibrium, the crust spins down faster than the core for ≈ 300 time units $\sim \tau_{\text{visc}}$, after which spin-down equilibrium is restored. This is similar to what we see during the set up of the initial condition. In Figure 2, we find $|\dot{\Omega}_2| > |\dot{\Omega}_1|$ for $t \lesssim 300$, and $|\dot{\Omega}_2| \approx |\dot{\Omega}_1|$ for $t \gtrsim 300$.

The evolution of $\Delta\Omega$ is different in the strong and weak mutual friction regimes in several ways. Firstly, the peak size of the glitch is larger for weak than strong mutual friction, with $\Delta\Omega_{\text{max}}^{\text{weak}} \approx 20\Delta\Omega_{\text{max}}^{\text{strong}}$. Secondly, while weak mutual friction produces a fast, monotonic rise followed by a slower, monotonic recovery, there is a noticeable oscillatory component in both the rise and recovery for $t \leq 30 \approx \tau_{\text{Ek}}$ with strong mutual friction. The oscillation period is ≈ 5 time units, similar to τ_{MF} , which may explain the absence of oscillation in the glitch with weak mutual friction: any oscillations which occur on a time-scale of $\tau_{\text{MF,weak}} = 500$ are in-

Parameter	Weak MF	Strong MF
$\Delta\Omega_1$	1.46×10^{-3}	2.09×10^{-3}
τ_1	0.98	1.80
$\Delta\Omega_2$	-3.90×10^{-2}	-3.73×10^{-2}
τ_2	70.3	63.5
$\Delta\Omega_p$	3.78×10^{-2}	3.55×10^{-2}

Table 3. Fitted parameters to equation (14) with $N = 2$ for the inner glitches in Figure 9 with strong ($B = 0.1$) and weak ($B = 10^{-4}$) mutual friction (MF) at $Re = 500$.

visible because $\Delta\Omega(t)$ decays exponentially on a time scale of $\tau_{2,\text{weak}} = 68$ (Table 2). Thirdly, the fitted rise time τ_1 is ~ 10 times faster with strong mutual friction than with weak, as shown in Table 2. However, looking at Figure 8, this is an artifact of the fit; $\Delta\Omega$ actually peaks at $t = 5.0$ and $t = 6.3$ for strong and weak mutual friction respectively, which corresponds to approximately one rotation period. Finally, weak mutual friction causes a permanent change in the spin frequency of the crust, viz. $\Delta\Omega_{\text{max}}^{\text{weak}}(t = 500)/\Delta\Omega_{\text{max}}^{\text{weak}} = 0.14$, c.f. $\Delta\Omega_{\text{max}}^{\text{strong}}(t = 500)/\Delta\Omega_{\text{max}}^{\text{strong}} = 0.003$. Though this result is not obvious in Figure 8, which truncates the recovery at $t = 100$ for clearer presentation of the oscillation, it can be seen clearly in the fitted values of $\Delta\Omega_p$ in Table 2, viz. $\Delta\Omega_p^{\text{weak}}/\Delta\Omega_{\text{max}}^{\text{weak}} = 0.14$ and $\Delta\Omega_p^{\text{strong}}/\Delta\Omega_{\text{max}}^{\text{strong}} = 0.005$.

5.5 Inner glitches

Inner glitches resemble crust glitches, except that Ω_1 jumps initially. The results below describe a glitch where Ω_1 is instantaneously increased to $\Omega_1(t = 0) = 1$, although in general we find that the size of the jump does not qualitatively change the recovery dynamics. Figure 9 plots the residual $\Delta\Omega$ for 500 time units following the glitch. The fitted parameters of a dual exponential fit are shown in Table 3. The recovery following an inner glitch is noticeably different from crust and bulk glitches. The glitch algorithm adds angular momentum to the system by increasing Ω_1 , which causes $v_p^\phi(r = R_1)$ and hence N_1 to also increase, increasing the spin-down torque on the core and upsetting spin-down equilibrium. The system returns to spin-down equilibrium after $t \approx \tau_{\text{visc}}$ by redistributing the added angular momentum from the glitch between $r = R_1$ and $r = R_2$, which also causes the crust to spin up. Figure 9 shows how, immediately following the glitch, $\Delta\Omega$ rises monotonically and asymptotes towards a maximum value after $t \sim 300 \sim \tau_{\text{visc}}$. There is no relaxation.

6 DISCUSSION

We discuss the above results in two groups. Firstly, we consider the crust and inner glitches, which can be grouped naturally, since both involve impulsive acceleration of a boundary and a net increase of the angular momentum of the system (section 6.1). Secondly, we consider the angular momentum-conserving bulk glitches (section 6.2).

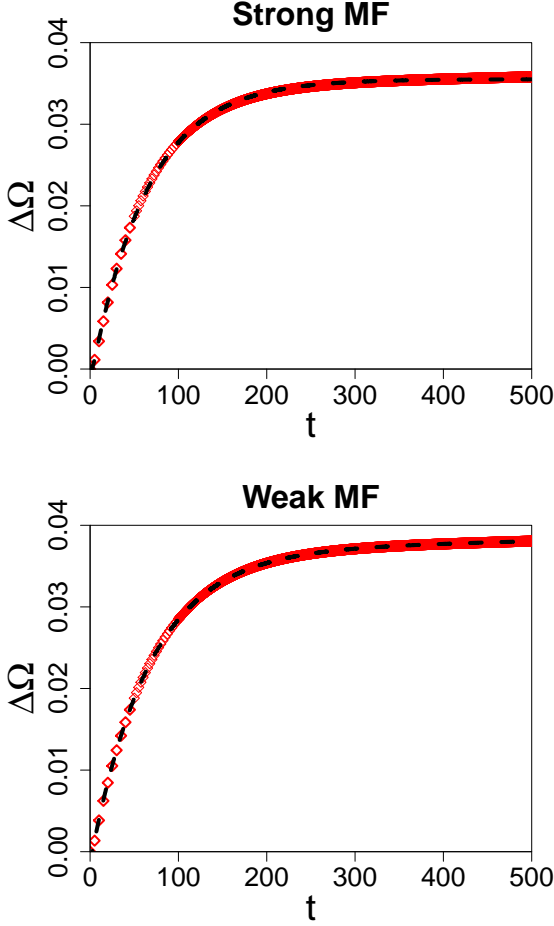


Figure 9. Angular velocity residuals, $\Delta\Omega(t) = \Omega_{2,g}(t) - \Omega_{2,ng}(t)$, for 500 time units following an inner glitch. The red diamonds show the data from the simulation. The black dashed curve shows a curve of best fit to a dual exponential recovery given by equation (14) with $N = 2$ (see Table 3 for values). In contrast to crust and bulk glitches, there is no relaxation following the spin up, $\Delta\Omega_{\max} = \Delta\Omega(t = 500)$. We see no significant difference in the recovery timescales between strong and weak mutual friction.

6.1 Crust vs inner glitches

A simple way to model the observed behaviour is by considering an idealised system consisting of four rigidly rotating components: the crust, the proton fluid, the neutron fluid, and the inner core, all of which may couple to or decouple from one another.

To describe crust glitches in this picture, we consider the inner core and the crust as being coupled prior to the glitch (see the discussion of spin-down equilibrium in section 4.2 and the bottom panels of Figure 2). The inertia of the neutrons and protons is small compared to the crust and core. The glitch is induced by suddenly spinning up the crust, upsetting spin-down equilibrium. A restoring force quickly spins down the crust and increases the angular velocity of the fluid and the core. Eventually, spin-down equilibrium is restored, and the permanent increase in the spin frequency of the crust can be estimated by multiplying the initial glitch size $\Delta\Omega_{\max} = \Delta\Omega(t = t_{\text{glitch}})$ by the ratio of the moments of inertia of the crust and the whole system, $I_{\text{crust}}/I_{\text{total}}$. For

inner glitches the argument is the same, but the relevant ratio is $I_{\text{core}}/I_{\text{total}}$, and $\Delta\Omega_{\max}$ is the amount by which the inner boundary spins up.

In Table 4 we compare the estimated permanent spin-up, $\Delta\Omega_p^{\text{est}} = \Delta\Omega_{\max} I_{\text{crust,core}}/I_{\text{total}}$ to the measured value of $\Delta\Omega(t = 500)$, as well as the fitted value $\Delta\Omega_p$ for crust and inner glitches with two different spin-down models described below. For the crust glitches, Table 4 shows that the estimated values agree approximately, though in both mutual friction regimes we obtain $\Delta\Omega(t = 500) \approx 1.1\Delta\Omega_p^{\text{est}}$. The discrepancy arises because the system is not completely coupled, even after 500 time units, so that the outer boundary is decelerating faster under the external torque than it would in equilibrium. In Table 4 we also consider the effect of adding a permanent change in the spin-down rate to our glitch recovery model, as such a change is often reported in the literature [e.g. Wang et al. (2000)]. $\Delta\Omega_p^{(5)}$ is the fitted value implied by equation (14), while $\Delta\Omega_p^{(6)}$ also includes a sixth parameter, the permanent change in the spin-down rate $\Delta\Omega_p t$ in equation (14). Both values agree to within 10%, both in comparison to each other and also to the predicted and observed values, and the sum-of-squares errors returned by the fitting algorithm for each model are similar.

6.2 Bulk glitches and mutual friction

An interesting result from the bulk glitch simulations is the large size difference between glitches with strong and weak mutual friction. Figure 5 shows that $|v_{\text{pn}}^{\phi}|$ is greater for weak mutual friction than strong, but the difference is at most a factor of ≈ 4 , not the factor of ≈ 20 observed in glitch sizes. To understand this discrepancy, we treat both fluid components and the boundaries as rigid bodies, so that the angular momentum of each is given by $I_x\Omega_x$, where the index $x = p, n$ or b denotes the protons, neutrons and boundary respectively. Conservation of angular momentum before and after the glitch implies

$$I_p\Omega_p^i + I_n\Omega_n^i + I_b\Omega_b^i = I_p\Omega_p^f + I_n\Omega_n^f + I_b\Omega_b^f, \quad (17)$$

where the superscripts i and f denote the initial (pre-glitch) and final (post-glitch) values respectively. Rearranging (17), we get

$$\Delta\Omega_b = -\frac{I_p}{I_b}\Delta\Omega_p - \frac{I_n}{I_b}\Delta\Omega_n, \quad (18)$$

where $\Delta\Omega_x = \Omega_x^f - \Omega_x^i$. If the proton fluid couples to the boundary much faster than the neutrons, so that the boundary spins up before being the neutrons recouple, then the effect of the neutrons can be neglected, and we can estimate the maximum glitch size as

$$\Delta\Omega_{\max}^{\text{est}} = \frac{\rho_p I_3 \langle v_{\text{pn}}^{\phi} \rangle_{\theta, \phi}^{\max}}{2I_2}. \quad (19)$$

For weak mutual friction, equation (19) yields $\Delta\Omega_{\max}^{\text{est}} = 3.8 \times 10^{-3}$, compared to $\Delta\Omega_{\max} = 4.6 \times 10^{-3}$ from the simulation. For strong mutual friction, the prediction is worse, $\Delta\Omega_{\max}^{\text{est}} = 1.2 \times 10^{-3}$, versus $\Delta\Omega_{\max} = 2.3 \times 10^{-4}$ from simulation. That the glitch size is overestimated with strong mutual friction is unsurprising, since setting $\Delta\Omega_n = 0$ in equation (19) implicitly assumes that the spin-up time is much greater than τ_{MF} , whereas actually the spin-up time is \approx one rotation period $\approx \tau_{\text{MF}}^{\text{strong}}$ [section 5.4]. In this regime,

Location	MF	$\Delta\Omega(t=500)$ ($\times 10^{-3}$)	$\Delta\Omega_p^{\text{est}}$ ($\times 10^{-3}$)	$\Delta\Omega_p^{(5)}$ ($\times 10^{-3}$)	$\Delta\Omega_p^{(6)}$ ($\times 10^{-3}$)
Crust	Strong	2.48	2.31	2.46	2.42
Crust	Weak	2.99	2.67	2.60	2.90
Inner	Strong	3.58	3.44	3.55	3.44
Inner	Weak	3.81	3.54	3.78	3.67

Table 4. We compare different methods for estimating the permanent change in the crust angular velocity residual, $\Delta\Omega_p$, following crust and inner glitches with strong and weak mutual friction. The third column estimates $\Delta\Omega_p$ as the value of $\Delta\Omega$ after 500 time units of simulation post-glitch, $\Delta\Omega(t=500)$. The fourth column estimates $\Delta\Omega_p$ using the formula $\Delta\Omega_p^{\text{est}} = \Delta\Omega_{\text{max}} I_{\text{crust,core}} / I_{\text{total}}$. Finally we estimate $\Delta\Omega_p$ by fitting the data to glitch recovery models similar to equation (14) with five parameters (fifth column) and six parameters (sixth column).

mutual friction suppresses spin up, limiting the size of a glitch. The oscillations with period $\approx \tau_{\text{MF}}^{\text{strong}}$ seen in the top panel of figure 8 may be related to the reduction in glitch size with strong mutual friction.

Another interesting result from the bulk glitch simulations is that weak mutual friction produces a permanent change in $\Delta\Omega$, while strong mutual friction restores the pre-glitch trend after 500 time units. During spin down, the neutron condensate is not affected by the spin-down torque initially, and only spins down with the crust and viscous component after a time $\sim \tau_{\text{MF}}$. At $t \lesssim \tau_{\text{MF}}$, the condensate spins down slower than the crust and viscous components, building up a ‘reservoir’ of angular momentum, $J_{\text{res}} = I_n |v_{\text{pn}}^\phi| / R_2$. With weak mutual friction, this reservoir grows at all times during the simulation, while with strong mutual friction it saturates.

When the glitch occurs, angular momentum is transferred from the ‘reservoir’ to the protons, which then spin up the crust. As discussed in section 5.3, spinning up the crust also increases the spin-down rate, so $\Delta\Omega$ decreases for $t \gtrsim 5$, until spin-down equilibrium is restored after $t \approx \tau_{\text{visc}} = 500$. Following a bulk glitch, the angular momentum of the overall system is unchanged, but the ‘observable’ $\Delta\Omega$ is the crust frequency, and the crust only couples to the neutrons when mutual friction is strong. When mutual friction is weak, the neutrons are decoupled from the crust, so the decrease in v_n^ϕ accompanying the increase in v_p^ϕ cannot be seen in $\Delta\Omega$, and the result of the glitch is an increase in the angular momentum of the observable components in the system.

This result has interesting implications in the context of the healing parameter, usually defined as (Wang et al. 2000)

$$Q = 1 - \frac{\Delta\Omega_p}{\Delta\Omega_{\text{max}}}, \quad (20)$$

so that $Q \rightarrow 0$ for a glitch that recovers fully, and $Q \rightarrow 1$ for a glitch with no recovery. Taking $\Delta\Omega_p = \Delta\Omega(t=500)$, we find $Q = 0.143$ with weak mutual friction and $Q = 0.003$ with strong mutual friction. Generally, Q is thought to be a measure of the relative moments of inertia of the inviscid and viscous components locked to the crust, but our results above indicate that mutual friction is important. Specifically, our results affect the standard argument, which holds that if some fraction of the superfluid with moment of inertia I_{res} spins down slower than the crust and viscous components, whose total moment of inertia is denoted I_c , then the ratio I_{res}/I_c provides an upper bound on the angular momentum which is ‘recovered’ by glitches, i.e. if $\dot{\Omega}_{\text{sd}}$ is the

average spin-down rate of a pulsar and $\dot{\Omega}_{\text{glitch}}$ is the average spin-up rate from glitches then $I_{\text{res}}/I_c \geq \dot{\Omega}_{\text{glitch}}/\dot{\Omega}_{\text{sd}}$. Often [e.g. Link, Epstein & Lattimer (1999); Andersson et al. (2012)], I_{res} estimated in this way is taken to be an indication of the superfluid fraction in the inner crust, is then used to put constraints on the nuclear equation of state. However, our simulations show that mutual friction affects the size of the reservoir more than ρ_n/ρ_p .

7 CONCLUSIONS

In this paper, we perform numerical simulations of pulsar glitches by solving the two-fluid equations of motion for the neutrons and protons in spherical Couette geometry. Glitches are simulated in three ways: firstly, by an instantaneous increase in the angular velocity of the crust; secondly, by an instantaneous increase in the angular velocity of the inner core; and thirdly, by instantaneously locking together the neutron and proton velocities throughout the interior. All three experiments start from a realistic initial state which is set up from initially corotating boundaries, after which the outer boundary is spun down by a constant torque on the crust for $\approx 10^2$ rotation periods. In all cases we observe that the angular velocity of the crust increases, but we find that the response of the crust angular velocity following a glitch varies depending on the way the glitch is activated. Glitches that originate in the crust exhibit an instantaneous angular velocity jump, followed by an exponential relaxation towards the pre-glitch trend. Glitches that originate in the core exhibit a permanent angular velocity increase building up over ≈ 50 rotation periods with no subsequent relaxation. Glitches that are caused by a sudden recoupling of the two fluid components in the bulk have a rise time that is similar to the rotation period of the star, followed by an exponential relaxation. Glitch sizes and the smoothness and completeness of the recovery are affected by the strength of mutual friction. The finding that different glitch activation mechanisms produce different kinds of recoveries may help to explain some of the diversity seen in the population of glitches (Wong, Backer & Lyne 2001; Espinoza et al. 2011; Haskell & Antonopoulou 2014).

Our results demonstrate the importance of mutual friction in bulk glitches. When mutual friction is strong, the lag between the two fluid components can reverse between $r = R_1$ and $r = R_2$, so that the neutron condensate spins down faster than the protons in some parts of the star. Mutual friction also affects the size of bulk glitches: with

stronger mutual friction glitches are smaller, and the recovery is non-monotonic, exhibiting oscillations with a period similar to the mutual friction time-scale which are damped after an Ekman time. As well as these interesting effects, we also find that mutual friction controls the healing parameter Q , a result which has implications for using pulsar glitches to test models of nuclear matter (Link, Epstein & Lattimer 1999; Andersson et al. 2012; Newton, Berger & Haskell 2015).

In order to preserve numerical stability and work with available computational resources, we necessarily make a number of simplifying assumptions. In particular, the choice of superfluid boundary conditions is an open question in the literature, which will be refined in light of future experimental and theoretical work. We also aim to improve the model in the future by including entrainment and vortex tension in the equations of motion and adapting the two-fluid solver to allow for non-uniform densities.

ACKNOWLEDGMENTS

This work was supported by Australian Research Council (ARC) Discovery Project Grant DP110103347. G. H. would like to thank Dr Carlos Peralta and Dr Eric Poon for their assistance with numerical simulations. G. H. acknowledges support from the University of Melbourne through via Melbourne Research Scholarship. B. H. acknowledges support from the ARC via a Discovery Early Career Researcher Award. Simulations were performed on the MASSIVE cluster² at Monash University, using computer time awarded through the National Computational Merit Allocation Scheme.

REFERENCES

- Adachi H., Fujiyama S., Tsubota M., 2010, *Phys. Rev. B*, 81, 104511
- Alpar M. A., 1977, *ApJ*, 213, 527
- Alpar M. A., Chau H. F., Cheng K. S., Pines D., 1996, *ApJ*, 459, 706
- Alpar M. A., Langer S. A., Sauls J. A., 1984, *ApJ*, 282, 533
- Anderson P. W., Alpar M. A., Pines D., Shaham J., 1982, *Philosophical Magazine, Part A*, 45, 227
- Anderson P. W., Itoh N., 1975, *Nature*, 256, 25
- Andersson N., Comer G. L., 2006, *Classical and Quantum Gravity*, 23, 5505
- Andersson N., Comer G. L., Prix R., 2004, *MNRAS*, 354, 101
- Andersson N., Glampedakis K., Ho W. C. G., Espinoza C. M., 2012, *Physical Review Letters*, 109, 241103
- Andersson N., Haskell B., Samuelsson L., 2011, *MNRAS*, 416, 118
- Andersson N., Sidery T., Comer G. L., 2006, *MNRAS*, 368, 162
- Andersson N., Sidery T., Comer G. L., 2007, *MNRAS*, 381, 747
- Bagchi P., Balachandar S., 2002, *Journal of Fluid Mechanics*, 466, 365
- Baggaley A. W., Barenghi C. F., 2012, *Journal of Low Temperature Physics*, 166, 3
- Bak P., Tang C., Wiesenfeld K., 1987, *Physical Review Letters*, 59, 381
- Baym G., Bethe H. A., Pethick C. J., 1971, *Nuclear Physics A*, 175, 225
- Baym G., Pethick C., Pines D., 1969, *Nature*, 224, 673
- Benton E., Clark Jr A., 1974, *Annual Review of Fluid Mechanics*, 6, 257
- Blaauwgeers R. et al., 2002, *Physical Review Letters*, 89, 155301
- Boyd J., 2013, *Chebyshev and Fourier Spectral Methods: Second Revised Edition*, Dover Books on Mathematics. Dover Publications
- Campbell L. J., Krasnov Y. K., 1982, *Journal of Low Temperature Physics*, 49, 377
- Canuto C., Hussaini Y., Quarteroni A., Thomas A. J., 1993, *Spectral Methods in Fluid Dynamics*, Scientific Computation. Springer Berlin Heidelberg
- Carter B., Chamel N., Haensel P., 2006, *International Journal of Modern Physics D*, 15, 777
- Chamel N., 2012, *Phys Rev C*, 85, 035801
- Chamel N., 2013, *Physical Review Letters*, 110, 011101
- Chandler E., Baym G., 1986, *Journal of Low Temperature Physics*, 62, 119
- Cheng K. S., Pines D., Alpar M. A., Shaham J., 1988, *ApJ*, 330, 835
- Dodson R., Lewis D., McCulloch P., 2007, *Ap&SS*, 308, 585
- Dodson R. G., McCulloch P. M., Lewis D. R., 2002, *ApJ*, 564, L85
- Donnelly R. J., 1991, *Quantized Vortices in Helium II*
- Elshamouty K. G., Heinke C. O., Sivakoff G. R., Ho W. C. G., Shternin P. S., Yakovlev D. G., Patnaude D. J., David L., 2013, *ApJ*, 777, 22
- Elzhov T. V., Mullen K. M., Spiess A.-N., Bolker B., 2013, *minpack.lm: R interface to the Levenberg-Marquardt nonlinear least-squares algorithm found in MINPACK, plus support for bounds*. R package version 1.1-8
- Espinoza C. M., Lyne A. G., Stappers B. W., Kramer M., 2011, *MNRAS*, 414, 1679
- Fetter A. L., 2009, *Reviews of Modern Physics*, 81, 647
- Glampedakis K., Andersson N., 2009, *Physical Review Letters*, 102, 141101
- Gorter C. J., Mellink J. H., 1949, *Physica*, 15, 285
- Hall H. E., Vinen W. F., 1956, *Royal Society of London Proceedings Series A*, 238, 215
- Haskell B., Andersson N., Comer G. L., 2012, *Physical Review D*, 86, 063002
- Haskell B., Antonopoulou D., 2014, *MNRAS*, 438, L16
- Haskell B., Melatos A., 2015, *International Journal of Modern Physics D*, 24, 30008
- Haskell B., Pizzochero P. M., Sidery T., 2012, *MNRAS*, 420, 658
- Heinke C. O., Ho W. C. G., 2010, *ApJ*, 719, L167
- Henderson K. L., Barenghi C. F., 1995, *Journal of Low Temperature Physics*, 98, 351
- Henderson K. L., Barenghi C. F., Jones C. A., 1995, *Journal of Fluid Mechanics*, 283, 329
- Hills R. N., Roberts P. H., 1977, *Archive for Rational Mechanics and Analysis*, 66, 43
- Hobbs G. B., Edwards R. T., Manchester R. N., 2006, *MN-*

² <https://www.massive.org.au/>

- RAS, 369, 655
- Khalatnikov I. M., Hohenberg P. C., 1965, An introduction to the theory of superfluidity. WA Benjamin New York
- Landau L. D., Lifshitz E. M., 1959, Fluid mechanics
- Lattimer J. M., Prakash M., 2004, Science, 304, 536
- Link B., 2012, MNRAS, 421, 2682
- Link B., Epstein R. I., Lattimer J. M., 1999, Physical Review Letters, 83, 3362
- Manchester R. N., Hobbs G., 2011, ApJ, 736, L31
- Manchester R. N., Hobbs G. B., Teoh A., Hobbs M., 2005, AJ, 129, 1993
- Mannarelli M., Rajagopal K., Sharma R., 2007, Phys. Rev. D, 76, 074026
- Mastrano A., Melatos A., 2005, MNRAS, 361, 927
- Melatos A., 1997, MNRAS, 288, 1049
- Melatos A., 2012, ApJ, 761, 32
- Melatos A., Howitt G., Delaigle A., Hall P., 2015, *in prep.*
- Melatos A., Peralta C., 2007, ApJ, 662, L99
- Melatos A., Peralta C., Wyithe J. S. B., 2008, ApJ, 672, 1103
- Mendell G., 1991, ApJ, 380, 515
- Middleditch J., Marshall F. E., Wang Q. D., Gotthelf E. V., Zhang W., 2006, ApJ, 652, 1531
- Migdal A. B., 1959, Nucl. Phys. A, 13, 655
- Nakabayashi K., Zheng Z., Tsuchida Y., 2002, Physics of Fluids (1994-present), 14, 3973
- Newton W. G., Berger S., Haskell B., 2015, MNRAS, 454, 4400
- Page D., Geppert U., Weber F., 2006, Nuclear Physics A, 777, 497
- Page D., Prakash M., Lattimer J. M., Steiner A. W., 2011, Physical Review Letters, 106, 081101
- Peralta C., 2006, PhD thesis, University of Melbourne
- Peralta C., Melatos A., 2009, ApJ, 701, L75
- Peralta C., Melatos A., Giacobello M., Ooi A., 2005, ApJ, 635, 1224
- Peralta C., Melatos A., Giacobello M., Ooi A., 2006, ApJ, 651, 1079
- Peralta C., Melatos A., Giacobello M., Ooi A., 2008, Journal of Fluid Mechanics, 609, 221
- Prix R., 2004, Physical Review D, 69, 043001
- Reisenegger A., 1993, Journal of Low Temperature Physics, 92, 77
- Ruderman M., 1969, Nature, 223, 597
- Ruderman M., 1976, ApJ, 203, 213
- Ruderman M., Zhu T., Chen K., 1998, ApJ, 492, 267
- Schwarz K. W., 1985, Phys. Rev. B, 31, 5782
- Seveso S., Pizzochero P. M., Grill F., Haskell B., 2014, ArXiv e-prints
- Shemar S. L., Lyne A. G., 1996, MNRAS, 282, 677
- Shternin P. S., Yakovlev D. G., Heinke C. O., Ho W. C. G., Patnaude D. J., 2011, MNRAS, 412, L108
- Sidery T., Passamonti A., Andersson N., 2010, MNRAS, 405, 1061
- Tilley D., Tilley J., 1990, Superfluidity and Superconductivity, Graduate Student Series in Physics. Taylor & Francis
- Turcotte D. L., 1999, Reports on Progress in Physics, 62, 1377
- van Eysden C. A., 2015, Journal of Fluid Mechanics, 783, 251
- van Eysden C. A., Melatos A., 2010, MNRAS, 409, 1253
- van Eysden C. A., Melatos A., 2011, Journal of Low Temperature Physics, 165, 1
- van Eysden C. A., Melatos A., 2013, Journal of Fluid Mechanics, 729, 180
- van Eysden C. A., Melatos A., 2014, Journal of Fluid Mechanics, 744, 89
- Wang N., Manchester R. N., Pace R. T., Bailes M., Kaspi V. M., Stappers B. W., Lyne A. G., 2000, MNRAS, 317, 843
- Warszawski L., Melatos A., 2011, MNRAS, 415, 1611
- Warszawski L., Melatos A., 2013, MNRAS, 428, 1911
- Warszawski L., Melatos A., Berloff N. G., 2012, Phys. Rev. B, 85, 104503
- Watkins N. W., Pruessner G., Chapman S. C., Crosby N. B., Jensen H. J., 2015, Space Sci. Rev.
- Weber F., Negreiros R., Rosenfield P., Stejner M., 2007, Progress in Particle and Nuclear Physics, 59, 94
- Wong T., Backer D. C., Lyne A. G., 2001, ApJ, 548, 447
- Yavorskaya I., Belyaev Y. N., Monakhov A., Astafeva N., Scherbakov S., Vvdenskaya N., 1980, NASA STI/Recon Technical Report N, 81, 25327
- Yu M. et al., 2013, MNRAS, 429, 688